A Comparative Evaluation of Rule-Based Strategies, ECMSs, and MPC Strategies for Fuel Cell Hybrid LCV Energy Management

World Electric Vehicle Journal

MDPI

Article

A Comparative Evaluation of Rule-Based Strategies, ECMSs, and MPC Strategies for Fuel Cell Hybrid LCV Energy Management

Zihao Guo, Elia Grano *, Henrique de Carvalho Pinheiro and Massimiliana Carello

Department of Mechanical and Aerospace Engineering, Politecnico di Torino, 10129 Turin, Italy; zihao.guo@polito.it (Z.G.); henrique.decarvalho@polito.it (H.d.C.P.); massimiliana.carello@polito.it (M.C.)
* Correspondence: elia.grano@polito.it

Abstract

Energy Management Strategies (EMSs) are crucial for enhancing fuel economy and reducing emissions in light commercial vehicles (LCVs). This paper presented three EMS approaches for LCVs with hybrid powertrains: Rule-Based Control (RBC) and two optimization-based strategies, the Equivalent Consumption Minimization Strategy (ECMS) and Model Predictive Control (MPC). To enhance robustness under varying operating conditions, optimization algorithms were designed and tuned using the WLTC City driving cycle, and adaptive components were included. For a fair assessment of overall efficiency, all strategies were compared under identical constraints on hydrogen and electrical energy consumption. The results showed that, under these constraints, MPC achieved the longest driving distance, highlighting its superior energy utilization capability. In a broader comparative analysis, both the ECMS and MPC outperformed the benchmark RBC, with MPC demonstrating the most consistent performance, enhanced stability, and strong adaptability in dynamic scenarios. The findings indicate that MPC offers notable advantages for LCV energy management, combining efficiency, robustness, and interpretability, positioning it as a promising candidate for practical implementation in future hybrid powertrain systems.

Keywords: adaptive energy management; fuel cell system; hybrid powertrain; consumption optimization strategy; model predictive control; rule-based control

Check for updates

Academic Editors: Joeri Van Mierlo, Vladimir Katic and Grzegorz Sierpiński

Received: 31 December 2025
Revised: 17 March 2026
Accepted: 19 March 2026
Published: 23 March 2026

1. Introduction

The transition toward sustainable urban and commercial mobility is accelerating the development of zero-emission vehicles. Hydrogen Fuel Cell Electric Vehicles (FCEVs) represent a promising solution for the LCV sector due to their high energy density, rapid refueling capability and zero noxious tailpipe emissions [1]. However, the commercialization of FCEVs still faces significant challenges, particularly regarding the durability of the fuel cell stack. Recent studies have emphasized the importance of advanced diagnostic techniques, such as polarization loss decomposition-based online State-of-Health (SoH) estimation [2], and life prediction models that account for the recovery phenomenon of reversible voltage loss [3]. While these studies highlight health-aware management, establishing a robust energy consumption baseline under off-design conditions remains a fundamental prerequisite.

To satisfy the highly dynamic power demands and efficiency requirements of LCV applications, hybrid powertrain architectures, integrating a Fuel Cell (FC) stack with a battery or supercapacitor, are commonly adopted [4]. The performance, efficiency, and

durability of such systems depend strongly on the EMS, which governs the real-time power split between the subsystems [5,6].

EMSs aim to allocate power between the FC system and the Energy Storage System (ESS) to maximize overall energy efficiency while mitigating the degradation of the FC stack [7], and these strategies broadly fall into three categories: rule-based, optimization-based, and Artificial Intelligence (AI)-based methods [8]. While AI techniques, such as Reinforcement Learning (RL), promise greater adaptability and performance by learning complex, model-free dynamics, their widespread adoption is hindered by high computational requirements, intensive training costs, and a lack of interpretability [9]. This study considers these practical constraints and builds upon the LCV model presented in [10], which includes a comparative assessment of three EMS approaches for hybrid LCV powertrains: a baseline RBC, ECMS and MPC.

RBC is a popular strategy for real-time energy management, relying on predefined rules and thresholds to manage power distribution between the FC and the battery [11]. These rules are typically based on factors like the battery State of Charge (SOC), the immediate power demand of the system, and other key operating parameters [12]. The development of these systems often incorporates advanced optimization; for instance, rule-based EMSs for FC hybrid trains have been developed based on the results from Dynamic Programming (DP) under various conditions [13]. Furthermore, techniques such as the genetic algorithm are employed to generate optimized rule-based EMSs, ensuring the optimization of power between the FC and the battery system [14]. But in this study, the RBC strategy is just considered a baseline, without further modification or optimization.

Optimization-based control designs the EMS by formulating it as an optimization problem, with the goal of finding optimal control actions that minimize a specific objective function [15]. Globally optimal methods, such as DP and Pontryagin's Minimal Principle (PMP), are commonly used because they theoretically provide the best possible solution [16]; for example, DP-based EMSs can reduce fuel consumption and battery degradation, while PMP-based EMSs often focus on hydrogen consumption reduction or maximizing fuel cell efficiency [17]. However, these global optimization approaches depend on prior knowledge of the future driving profile and involve high computational demand, both of which restrict their applicability to real-time control in complex systems [18,19]. Local optimization methods, such as ECMSs, are attractive for dynamic, real-time control due to their faster computation, although this speed comes at the cost of not guaranteeing a globally optimal solution [20].

MPC is considered a state-of-the-art algorithm, initially utilized for speed control applications due to its excellent real-time responsiveness [21]. Through accurate system modeling, MPC has also proven to be suitable for energy management algorithms, where adjustable weighting factors can be used within the optimization problem to tune control objectives [22,23]. Although fuel cell commercialization remains hindered by challenges such as cost, cold start performance, and durability [24], the flexible framework of MPC provides opportunities to address these issues by incorporating validated behavioral models directly into the cost function. Furthermore, techniques such as Response Surface Methodology (RSM) have been employed for model correction and refinement [25,26]. This sophisticated approach allows MPC to achieve efficient and effective control, even when dealing with complex nonlinear models [27].

Real-world driving is characterized by variable and unpredictable operating conditions. Prior experimental studies highlight substantial discrepancies between standardized test cycles and real operation [28]. Motivated by this, the present work incorporates adaptive formulations of both ECMSs and MPC from the outset, enabling the algorithms to

adjust their behavior based on instantaneous driving conditions and vehicle states [29]. This adaptability is essential for ensuring robust performance beyond idealized scenarios [30,31].

The evaluation relies on a simulation framework developed in MATLAB/Simulink R2025a. All strategies are first assessed under the WLTC City cycle as the reference, which is an essential subset of the Worldwide Harmonized Light-Duty Test Cycle (WLTC), comprising only the low- and medium-speed phases [32]. It is specifically characterized by frequent stops and starts and high dynamic variations at low average speeds, realistically reflecting congested urban traffic [33]. Given that LCVs are predominantly used for city logistics and urban services, the WLTC City cycle serves as a relevant and practical standard for evaluating the energy consumption, emissions, and all-electric range of hybrid LCV powertrains operating in their typical environment [34]. The comparison is then extended to off-design scenarios using a set of fifty distinct driving cycles generated through a Simulink add-on called Powertrain Blockset [35].

The principal performance indicator is the total driving distance given identical energy consumption, providing an indirect measure of overall energy efficiency [36]. The analysis also accounts for practical constraints relevant to LCV implementation, including limitations imposed by the Vehicle Control Unit (VCU) such as computational requirements and restrictions on rapid power transients to preserve fuel cell longevity.

Table 1 summarizes representative state-of-the-art studies and highlights three overarching limitations in current FCEV EMS research: the mismatch between control-oriented models and real system physics, energy evaluation biases introduced by equivalence-based metrics, and limited robustness validation beyond standardized cycles.

Table 1. Comparative analysis of recent FCEV energy management research.

Reference	Methodology	Discontinuous FC Power	Dwell-Time Constraint	Energy Metric Employed	Robustness Testing
PMP-DCR (2024) [37]	Optimization (PMP + Driving Cycle Recognition)	Yes (Idling/Startup penalties)	No	Equivalent Hydrogen Consumption	Combined standard cycles
Rule-based (2022) [38]	Adaptive Six-Step	No	No	Total Hydrogen Consumption and Total Driving Range	Loaded vs. unloaded mass variation
AHA-ECMS (2024) [39]	Hybrid Optimization (ECMS + Hummingbird)	No	No	Hydrogen Consumption	Standard FTP-75 driving profile
Robust JS (2025) [40]	Robust Min-Max (Jellyfish Search)	No	No	Hydrogen Consumption	Worst-case uncertainty
SSA-LSTM P-ECMS (2025) [41]	Learning-Based Predictive ECMS	No	No	Equivalent Hydrogen Consumption	C-WTVC and NREL2VAIL cycles

To address these challenges, this work establishes a physics-consistent, hardware-constrained evaluation benchmark for FCEV energy management. A key distinguishing feature of the proposed framework is the explicit enforcement of two hardware-level constraints characteristic of the industrial prototype under study: a discontinuous FC operating domain (idle: 1.5 kW; active: 20 ÷ 70 kW) and a mandatory minimum dwell-time of 10 s in each operating mode, both enforced at the VCU level. As shown in Table 1, no existing study simultaneously accounts for both constraints, making this framework a necessary complement to existing comparative work. Performance is evaluated through a multi-

tiered methodology combining the WLTC City cycle, unbiased energy benchmarking based on total driving distance, and robustness testing across 50 off-design driving scenarios. The ultimate objective is to identify the EMS most suitable for further development in a Hardware-in-the-Loop (HIL) environment and subsequent VCU integration.

2. Test Environment

Before comparing different control strategies for EMSs, it is necessary to define the simulation environment used for their integration and assessment [42]. This paragraph introduces the fundamental elements required for functional validation and performance evaluation, with a particular emphasis on the vehicle model and the representative driving cycles. A reliable simulation platform is essential for analyzing the behavior of various EMSs. The integrated environment adopted was implemented in MATLAB/Simulink R2025a and incorporates a detailed vehicle model capable of reproducing the physical behavior of the vehicle, its energy flow dynamics, and the key operational characteristics of the hybrid powertrain [10]. In addition, the driving cycles selected for the analysis are presented, as they provide standardized conditions for assessing fuel economy, energy consumption, and overall performance across different EMSs.

The outlines and justifications of the adopted vehicle model and the driving cycles are presented.

2.1. Vehicle Model

EMSs are applied to an FCEV model, representing an LCV, as shown in Figure 1.

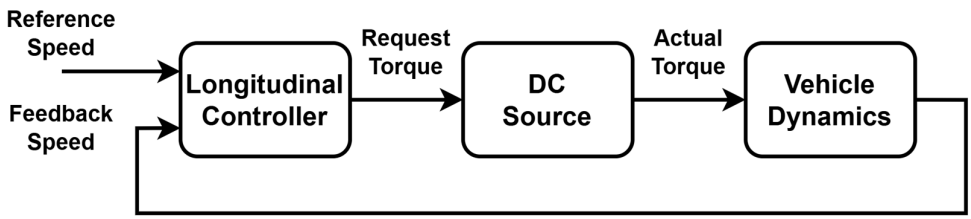

Figure 1. Vehicle model schema.

The reference vehicle speed obtained from the driving cycle and the feedback vehicle speed computed by the vehicle dynamic model are provided as inputs to the longitudinal controller. A PID-based control strategy is employed to mimic driver behavior by minimizing the speed tracking error. Based on this error, the controller generates a pedal command, which can also be interpreted as an equivalent torque demand.

This torque demand is transmitted to the DC source subsystem, which includes Electric drive (E-Drive) and energy sources. Within this subsystem, the EMS is implemented to allocate the required power among the available energy sources and to simulate the generation of the actual traction torque. The resulting torque is then applied to the Vehicle Dynamic System (VDS), which models the longitudinal vehicle behavior and computes the vehicle acceleration, speed, and traveled distance. The simulated vehicle speed is finally fed back to the longitudinal controller, forming a closed-loop control structure that enables the accurate tracking of the reference driving cycle.

2.1.1. Fuel Cell System

The FC system model incorporates both electrochemical dynamics and auxiliary component modeling. It was calibrated based on empirical data to accurately capture dynamic variations in power and efficiency in response to changes in power demand. Table 2 presents the basic specification. The current, i_{FC}, is defined as the input to the model, while the output quantities are the FC voltage, v_{FC}, and the net power, P_{FC}. Considering

the characteristic slow response of the FC voltage to sudden transients, at each time step, t, the electrical relationship is expressed as follows [43]:

$$i_{FC}(t) = \frac{P_{FC}(t)}{v_{FC}(t-1)} \tag{1}$$

where v_{FC} is computed at each time step as a nonlinear function of the current density, accounting for reversible voltage and electrochemical loss mechanisms [10]. Considering the slow dynamic response of the fuel cell voltage, the current density is evaluated using a discrete time step of 0.01 s. This step size is sufficiently smaller than the dominant electrochemical and gas transport time constants [44], enabling accurate voltage estimation while ensuring numerical stability and consistency. Assuming stoichiometric balance and complete reaction, the required hydrogen mass flow rate, $\dot{m}_{H_2}$, can be calculated by the following equation [45]:

$$\dot{m}_{H_2} = M_{H_2} \cdot \frac{n \cdot i_{FC}}{2F} \tag{2}$$

where M_{H_2} is the molecular mass of hydrogen, n is the number of cells and F is the Faraday number.

Table 2. Fuel cell technical specification.

Metric	Value
System net power	Max. 70 kW
Cells	440 cells
Active cell area	270 cm^2
Output current	Max. 300 A
Plate thickness (anode/cathode)	0.1 mm
Weight	175 kg

The overall total efficiency η_{FC} of the FC system follows the relationship below [46]:

$$\eta_{FC} = \frac{P_{FC,net}}{\dot{m}_{H_2} \cdot Q_L} \tag{3}$$

where $P_{FC,net}$ is the net power of the FC stack, and Q_L is the lower heating value of hydrogen.

Compared to purely static lookup table methods, this dynamic modeling approach introduces a penalizing effect during periods of rapid power changes, though its impact on the total integrated energy consumption is not particularly pronounced. It is acknowledged that degradation is also influenced by thermal management [47] and adaptive SoH temperature sensitivity [48]. To maintain a clear focus on the comparative assessment of RBC, ECMS, and MPC algorithms, and due to the current absence of long-term experimental degradation data, these complex factors are not integrated into the current plant model to avoid over-parameterization.

2.1.2. Battery

Given limitations in available empirical data, the battery pack is modeled using a combination of the equivalent circuit method and a steady-state lookup table approach. Table 3 presents the technical specification of the battery. The key electrical parameters, the battery open circuit voltage, v_{nom}, and the internal resistance, R_{int}, are defined as static functions of the SoC and temperature, typically implemented via multi-dimensional lookup tables. For simplification, thermal behavior is neglected: the cell temperature is assumed to be constant at an ambient temperature of 25 °C.

Table 3. Battery technical specification.

Metric	Value
Cells in series	96 units
Cells in parallel	2 units
Nominal cell voltage	3.7 V
Nominal cell capacity	52 Ah
Cell mass	750 g
Ohmic internal resistance	0.8 mΩ

The battery terminal voltage, v_{batt}, is determined by the following [49]:

$$v_{bat} = v_{nom} - i_{bat} \cdot R_{int} \tag{4}$$

$$P_{bat} = v_{bat} \cdot i_{bat} \tag{5}$$

The calculation of the battery SoC is determined by taking the initial SoC value SoC_0 and subtracting the cumulative charge variation over time:

$$SoC(t) = SoC_{t_0} - \int_{t_0}^{t} \frac{i_{bat}(\tau)}{C_{bat}} \cdot d\tau \tag{6}$$

The battery capacity, C_{bat}, is temperature-dependent in real applications but treated as a constant parameter in this model.

The battery discharge and charge current limits are implemented using a lookup table that is a function of the SoC and temperature, ensuring the model respects the operating safety limits. The current model simplifies the thermal dynamic process (such as the battery isothermal assumption), and in the future, the accuracy of multi-physics simulation can be improved by coupling advanced thermal management strategies, especially under WLTC high-frequency transient conditions.

2.1.3. Electric Drive

The E-Drive system is modeled using a quasi-static efficiency map approach [50]. Efficiency, η_{em}, is characterized by a two-dimensional lookup table as a function of output torque, T_{em}, and rotational speed, ω_{em}:

$$\eta_{em} = f(T_{em}, \omega_{em}) \tag{7}$$

The actual mechanical torque output delivered to the VDS is calculated from the mechanical power and rotational speed:

$$T_{em} = \frac{P_{mech}}{\omega_{em}} \tag{8}$$

The E-Drive can operate as either a motor (traction) or a generator (regeneration). The relationship between electrical power, P_{elec}, and mechanical power, P_{mech}, is defined by applying efficiency based on the operating mode [51]:

$$\begin{cases} P_{elec} = P_{mech} \cdot \eta_{em}, & Regeneration \\ P_{elec} = P_{mech} / \eta_{em}, & Traction \end{cases} \tag{9}$$

2.1.4. Vehicle Dynamics

As the focus of this study is exclusively on energy distribution and comparison based on total travel distance, only the longitudinal dynamics of the vehicle are considered.

Considering a combination of aerodynamic drag and rolling resistance, the longitudinal resistive force, F_{xr}, is as follows [52,53]:

$$F_{xr} = A + B \cdot V + C \cdot V^2 \tag{10}$$

where the coefficients A, B, and C are determined experimentally by the prototype manufacturer through fitting to real-world driving data. These manufacturer-provided parameters are considered reliable for the purposes of this study.

The quadratic relationship (10) highlights how resistance components scale with speed, significantly impacting vehicle dynamics and energy consumption.

Assuming a rear-wheel drive configuration, the maximum tractive torque output at the wheel, T_{lim}, can be determined from a force/torque balance equation [54]:

$$T_{lim} = (a_v \cdot h_{CG} \cdot M/b + Mg \cdot a/l \cdot \cos\alpha) \cdot \mu_x \cdot r_w \tag{11}$$

where a_v is the longitudinal acceleration; g is gravitational acceleration; α is the road slope angle; The main parameters of the vehicle longitudinal dynamic model are summarized in Table 4.

Table 4. Vehicle longitudinal dynamic model parameters.

Parameters	Value
A	287.4 N
B	6.680 N/(km/h)
C	0.107 N/(km/h)^2
a	2275 mm
h_{CG}	0.8 m
l	4350 mm
M	5 ton
μ_x	1.21
r_w	0.372 m

Note: Similar to the Daily 7-ton model in the external configuration but not fully loaded.

2.1.5. Longitudinal Controller

In powertrain simulations, the longitudinal control module functions as a virtual driver by regulating vehicle speed and acceleration to track a given reference profile. The controller evaluates the deviation between the target and actual speeds to determine the required acceleration or deceleration, which is subsequently translated into a motor torque demand through a torque reference generator. To maintain control stability, an anti-windup proportional–integral (PI) strategy is adopted. The resulting command signal can be expressed as follows [55]:

$$cmd(t) = V_{ref}(t) \cdot \frac{K_{ff}}{v_{nom}} + e_v(t) \cdot \frac{K_p}{v_{nom}} + \int_0^t \left(e_v(\tau) \cdot \frac{K_i}{v_{nom}} + e_{cmd}(\tau) \cdot K_{aw} \right) \cdot d\tau + \alpha(t) \cdot K_g \tag{12}$$

where V_{ref} denotes the reference vehicle speed and cmd represents the controller output. The road grade is given by α. The term e_v corresponds to the vehicle speed tracking error, while e_{cmd} denotes the command error. The parameters K_{ff}, K_p, and K_i represent the feedforward, proportional, and integral gains, respectively. In addition, K_{aw} is the anti-windup gain, and K_g is the gain associated with road grade compensation.

The control variable cmd is defined over the continuous range of $[-2, 1]$ to facilitate the transition between vehicle driving and braking modes. Within this framework, the interval $[0, 1]$ signifies the acceleration phase, directly mapping to the accelerator pedal

opening. Conversely, the negative range [−2, 0] governs deceleration, which is divided into two distinct stages to manage hybrid braking sources: the sub-interval [−1, 0] is dedicated to regenerative electric braking, while [−2, −1] activates mechanical friction braking. In both deceleration segments, the magnitude represents the utilization of the respective maximum torque from 0% to 100%. Based on this mapping logic, the input cmd is decomposed into three functional components, cmd_{accel}, cmd_{decel}, and cmd_{brake}, allowing for precise coordination between the powertrain and the foundation braking system. The torque command Trq_{ref} to the electric motor is defined as follows:

$$Trq_{ref} = cmd_{accel} \cdot Trq_{peak} + cmd_{decel} \cdot Trq_{const} \cdot R_{lim} \tag{13}$$

The maximum and continuous torque capabilities are described by T_{peak} and T_{const}, corresponding to acceleration and deceleration conditions, respectively. In this work, the regeneration limit coefficient R_{lim} is chosen as 0.5.

Regenerative braking is utilized as the primary deceleration mechanism under low braking demand, allowing kinetic energy to be recovered. In contrast, for high braking demand, the mechanical braking system supplements the required torque. This coordination strategy prioritizes energy recovery while reducing reliance on friction brakes. Additional modeling details are available in [10].

2.2. Test Cycles

Drive cycles are standardized speed–time traces essential for assessing vehicle performance and achieving regulatory certification (e.g., emissions, fuel economy). For LCVs, selecting a representative cycle is crucial to accurately predict real-world energy consumption and range, especially for urban logistics tasks [42].

The WLTC City cycle was selected because the vehicle model represents an LCV operating primarily in urban and suburban areas. This cycle is derived from the full WLTC Class 3 cycle but specifically excludes the high-speed/motorway section [33]. Its maximum speed is limited to approximately 95 km/h, making it representative of the required low-to-medium-speed operating environment for LCVs for delivery.

To broaden the assessment, a large set of cycles from the Simulink library [35] was filtered. All modal (steady state) cycles were excluded as they lack the transient dynamics of real-world driving and offer poor representativeness for energy management analysis [56]. Cycles with extremely low speeds were also dismissed as they were inefficient for generating meaningful energy statistics. The final set of fifty cycles provides a robust collection of transient driving patterns for a statistical comparison of total energy consumption and mileage [57].

3. Energy Management System Design

This section addresses the formulation and optimization of the three distinct control methodologies introduced in Section 1. The RBC strategy is designed based on predefined, fixed operating constraints. Both the ECMS and MPC require an optimization phase, where key parameters must be tuned to maximize performance over the targeted WLTC City drive cycle. Upon the completion of this design and optimization process, all three algorithms will be prepared for a formal comparative performance assessment.

3.1. EMS Architecture

The EMS structure handles the vehicle's power requirement through distinct parts. As shown in Figure 2, it starts with the Demand Layer, where a fast PID controller turns the driver's request for wheel torque into the total power needed from the main battery line. The power target then proceeds to the Power Split Layer, which serves as the core

management decision unit. It determines the optimal distribution of the required power between the fuel cell and the battery. The strategies are subject to formal performance evaluation to quantify the trade-offs in fuel efficiency and total attainable distance under identical operating conditions.

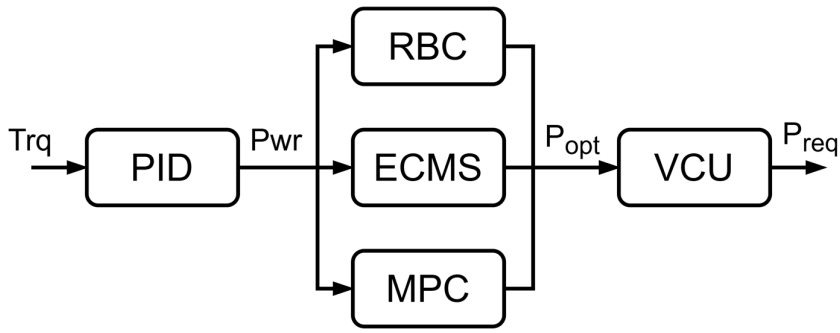

Figure 2. EMS control schema.

A Safety Check Layer is placed after this, applying direct limits set by the VCU to protect the hardware. These rules include stopping the fuel cell from running if the battery SoC is over 85%. Also, because of hardware issues at low power, any demand for FC power under 20 kW is automatically changed to 1.5 kW. For the operating condition of the FC, power equal to 1.5 kW as the "idle" state and power exceeding 20 kW as the "active" state were defined. To prevent rapid changes in the operating conditions from damaging the FC, a mode switch can only occur after the system has continuously operated in the current mode (either idle or active) for a minimum duration of 10 s.

While this safety limit is applied, it will likely reduce the perfect performance of advanced methods like MPC. However, if MPC can still show benefits even with these tough real-world rules, it strongly suggests that more advanced MPC can be designed later to specifically work around these system limits.

3.2. Rule-Based Control

The FC is activated to run continuously at a rated power level determined by the current SoC. This dynamic operation allows the FC to meet demands from the Power Control Unit (PCU) while also using any excess energy to recharge the battery. To manage this, a predefined reference, reported in Table 5, establishes the required FC output power, $P_{fc,std}$, based on the SoC. Additionally, the FC stack provides power according to direct demands from the inverter. This integrated approach ensures the FC covers immediate power needs and helps maintain the long-term battery charge.

$$\begin{cases} P_{fc} = P_{fc,std} + P_{fc,add} \\ P_{batt} = P_{req} - P_{fc} \end{cases} \tag{14}$$

$$\begin{cases} P_{fc,add} = \alpha \cdot \left(P_{fc,max} - P_{fc,std} \right) \\ \alpha = min\left(max\left(\frac{P_{req}}{120}^2, 0 \right), 1 \right) \end{cases} \tag{15}$$

where $P_{fc,std}$ is the standard FC power contribution, and $P_{fc,add}$ is the addition contribution due to the inverter power. α is the coefficient of the addition contribution.

Table 5. Standard FC power request under different SoC conditions.

SoC (%)	0	20	30	40	50	60	70	80	85	90	100
Power (kW)	70	70	70	70	35	25	20	18	0	0	0

3.3. Equivalent Consumption Management Strategy

The ECMS is a quasi-optimal instantaneous optimization strategy designed to minimize the combined equivalent consumption of hydrogen and electrical energy at each time step [58]. The method introduces the equivalence factor, s, which converts the battery electrical energy usage into an equivalent hydrogen consumption. When s is optimally tuned for a specific driving cycle, the ECMS guarantees the globally optimal power split under the defined constraints.

An optimal FC power request, $P_{FC,\,opt}$, is calculated to minimize the energy consumption of the hybrid powertrain [59]:

$$P_{FC,\,opt} = \underset{P_{FC}}{argmin}\left(\dot{m}_{H_2,eq}(P_{FC})\right) \tag{16}$$

where P_{FC} is the output power of the FC at the DC bus, and the equivalent energy consumption of the powertrain $\dot{m}_{H_2,eq}$ is as follows [29]:

$$\dot{m}_{H_2,eq} = \dot{m}_{H_2} + s \cdot \frac{P_{bat}}{LHV_{H_2}} \cdot p \tag{17}$$

where $\dot{m}_{H_2,eq}$ includes both hydrogen consumption $\dot{m}_{H_2}$ and battery output, in terms of battery equivalent hydrogen consumption $s \cdot P_{bat}/LHV_{H_2}$. The coefficient p is the penalty factor for SoC deviation from the prescribed reference, defined as follows:

$$p(SoC(t)) = 1 - \left(\frac{SoC(t) - SoC_{ref}}{(SoC_{max} - SoC_{min})/2}\right)^a \tag{18}$$

where SoC_{max} and SoC_{min} are the upper and lower thresholds of the battery; a is a constant value of the exponent, which is set equal to 3; and SoC_{ref} is the reference value of the battery SoC.

For a standard ECMS implementation on a fixed cycle, s is held constant [60], but its value must be tuned to ensure global consumption optimization over the entire cycle length. The determination of s was conducted through an offline calibration procedure aimed at minimizing equivalent fuel consumption while strictly satisfying the charge-sustaining requirement over the given long-distance driving cycle [61].

Given the convex relationship between s and the overall equivalent fuel consumption, a narrow-range grid search method was utilized to efficiently locate the optimum. Discrete values of the parameter s were selected within the estimated optimal region and evaluated through simulations, and the resulting relationship between s and total distance was approximated using curve fitting to obtain a continuous functional representation. The optimal solution, s, was identified by locating the global maximum of the resulting fitted curve, which is shown in Figure 3.

3.4. Model Predictive Control

At each time step k, MPC utilizes a predictive model of the FCHEV's dynamics to forecast the system's behavior over a finite prediction horizon, N_p. It calculates an optimal sequence of control actions (the power split trajectory) that minimizes a predefined cost function over this horizon [62]. Only the first calculated control action is applied to the system, and the entire optimization is repeated at the next time interval, effectively compensating for any model inaccuracies or unpredicted disturbances.

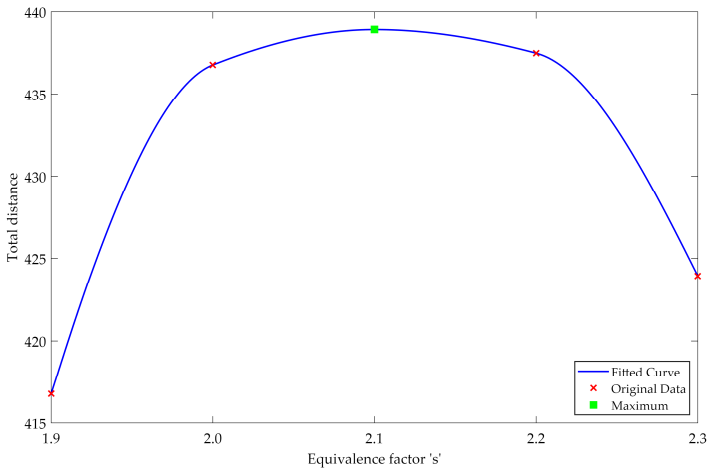

Figure 3. Optimization of equivalence factor.

The adopted mathematical model is constituted by the combination of Equations (19) and (20):

$$p(SoC(t)) = 1 - \left(\frac{SoC(t) - SoC_{ref}}{(SoC_{max} - SoC_{min})/2} \right)^a \tag{19}$$

$$\dot{SoC} = \frac{i_{bat}}{C_{bat}} = \frac{P_{bat}}{v_{bat} \cdot C_{bat}} \tag{20}$$

The DC system model can be transformed into a state-space representation as follows:

$$\begin{cases} \dot{x} = Ax + Bu \\ y = Cx + Du \end{cases} \tag{21}$$

where $x = [SoC,\ P_{DC}]^T$ is the state vector, and $u = [P_{bat},\ P_{FC}]^T$ is the control input vector. Meanwhile, the state-space model is discretized for the MPC design as follows:

$$\begin{cases} x(k+1) = A_d \cdot x(k) + B_d \cdot u(k) \\ y(k) = C_d \cdot x(k) + D_d \cdot u(k) \end{cases} \tag{22}$$

$$A_d = \begin{bmatrix} 1 & 0 \\ 0 & 0 \end{bmatrix},\ B_d = \begin{bmatrix} (v_{bat} \cdot C_{bat})^{-1} & 0 \\ 1 & \eta_{DC-DC} \end{bmatrix}, \\ C_d = \begin{bmatrix} 1 & 0 \\ 0 & 1 \end{bmatrix},\ D_d = \begin{bmatrix} 0 & 0 \\ 0 & 0 \end{bmatrix} \tag{23}$$

where A_d and B_d are the discrete time state-space matrices obtained from A and B, using the Zero-Order Hold (ZOH) method and $C_d = C$.

The cost function of MPC is as follows [27]:

$$J = \sum_{k=1}^{N_p} \left(\left(y_k - y_{ref} \right)^T Q \left(y_k - y_{ref} \right) + u_k^T R u_k \right) + \sum_{k=2}^{N_p} (u_k - u_{k-1})^T S (u_k - u_{k-1})$$

where N_p is the prediction horizon, and $Q = [q_1,\ q_2]^T$, $R = [r_1,\ r_2]^T$ and $S = [s_1,\ s_2]^T$ represent the diagonal weight matrices associated with the system states, control inputs, and control input increments, respectively, that define the controller's priorities.

For MPC, the optimization problem is also subject to several constraints, such as the upper and lower limitations of the SoC level, battery current and the FC power. The optimization solver incorporates all physical limitations directly into the problem formulation.

To systematically determine the optimal weighting parameters within the MPC cost function, we employed RSM, which is a statistical and mathematical technique that efficiently identifies the optimal relationship between input parameters (weights) and energy consumption (in terms of total distance) through experimental design and modeling.

Given the linear correlation between the SoC and the nominal voltage v_{nom}, it is hypothesized that, under the correct MPC operation, the influence of the reference SoC on the total travel distance will also be linear. The simulation results, obtained by systematically varying SoC_{ref} while keeping all other operating parameters constant, confirmed this trend. In Figure 4, values are parameterized as a percentage change relative to the baseline at a 20% SoC reference. There is a positive correlation between the SoC reference and the total distance achieved. Increasing the SoC reference from 20% to 80% results in a total distance improvement of 2.5%.

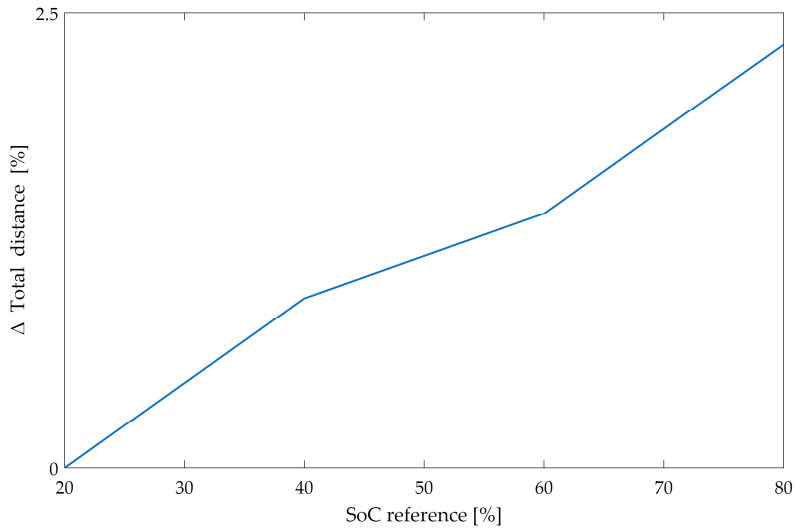

Figure 4. Sensitivity of total distance to SoC reference.

The fundamental principle governing MPC parameterization is that control performance is strongly affected by the relative proportions of the weighting matrices, rather than their absolute magnitudes. The core of the MPC optimization problem involves balancing the minimization of tracking error, Q, against the control effort constraints, R. Since the MPC cost function was normalized in terms of units, this focus allows for the simplification of complex weight matrix optimization into a targeted search focused on key scaling factors, such as the ratio with respect to Q and R. Moreover, recognizing that extreme ratios result in unacceptable performance imposes a physical constraint that effectively reduces the search space to a narrow core region.

This preliminary assumption significantly boosts the efficiency and convergence of RSM simulation load, since RSM commonly relies on efficient, three-level experimental designs. To satisfy the requirement for steps suitable for RSM coded levels (−1, 0, 1), the parameters were subjected to a logarithmic transformation, shown in Table 6, defined as $X = \ln(x)$. The optimal operating point is graphically presented on the response surface in Figure 5, and the optimal absolute parameter values, which are theoretically expected to yield the longest total travel distance, are calculated using the inverse exponential function $x = e^X$.

Table 6. Experimental variables and their coded and actual levels used in the RSM design.

Variable	Symbol	Transformation Equation	Low Level (−1)	Central Level (0)	High Level (+1)
Logarithmic Ratio of Q	X_1	$X_1 = ln(q_1/q_2)$	$ln(1)$	$ln(5)$	$ln(25)$
Logarithmic Ratio of R	X_2	$X_2 = ln(r_1/r_2)$	$ln(1)$	$ln(3)$	$ln(9)$

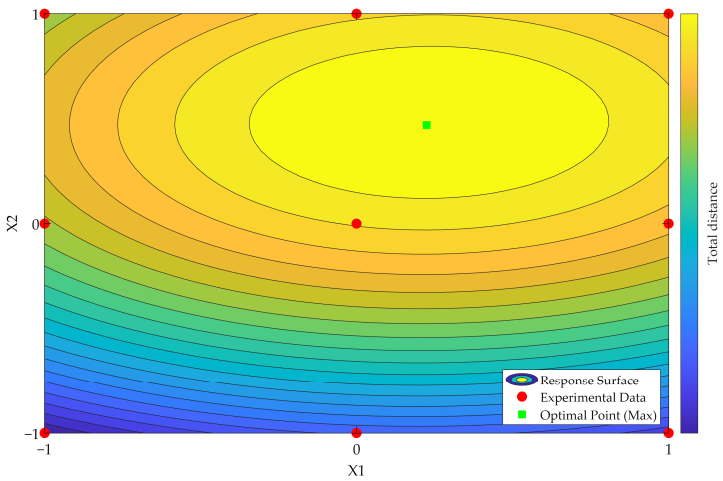

Figure 5. A contour plot of the total distance vs. X1 and X2, with the optimal point.

4. Performance Comparison

Comparative simulations were performed for RBC, the ECMS, and MPC. The initial conditions were standardized across all runs: a battery SOC of 90% and a full hydrogen tank. The simulation ended up reaching a final battery SOC of 10% and an empty hydrogen tank. With the total energy consumption being identical for all compared EMSs, the resulting total traveled distance serves as a direct metric for the average energy efficiency of each strategy. Under this unified energy constraint, a longer achievable distance directly corresponds to lower overall energy consumption and higher system-level efficiency. This metric avoids the need for arbitrary weighting between hydrogen and electrical energy and provides a physically intuitive indicator of real-world vehicle usability for fuel cell hybrid LCVs.

Figure 6 illustrates the battery SoC among the three controllers. Under an identical SoC_{ref}, both the RBC strategy and ECMS exhibit instantaneous control, leading to the superior tracking of SoC_{ref}. The ECMS maintains a higher average battery SOC, indicating better battery performance utilization and higher overall efficiency, which translates to a longer total distance traveled. MPC operates with a lower average battery SOC; however, it utilizes a wider battery operating range. This wider range provides a necessary buffer for the fuel cell system's operation, thus maximizing overall energy efficiency and resulting in the longest total distance traveled.

As the driving cycle is periodically repeated over the simulation horizon, the ESS response exhibits repeated patterns across individual and multiple cycles. To improve the clarity of the results and avoid excessive plot congestion that may hinder interpretation, a representative segment of the simulation is extracted and presented in a zoomed-in view. This approach facilitates a clearer and more detailed analysis of the dynamic interactions between the fuel cell and the battery, which may not be readily observable in the full-scale simulation results.

Figure 7 displays the operational performance of MPC. Since the controller accounts for future states rather than merely seeking immediate local optimization, it effectively smoothens FC power fluctuations and maintains operation within a high-efficiency regime.

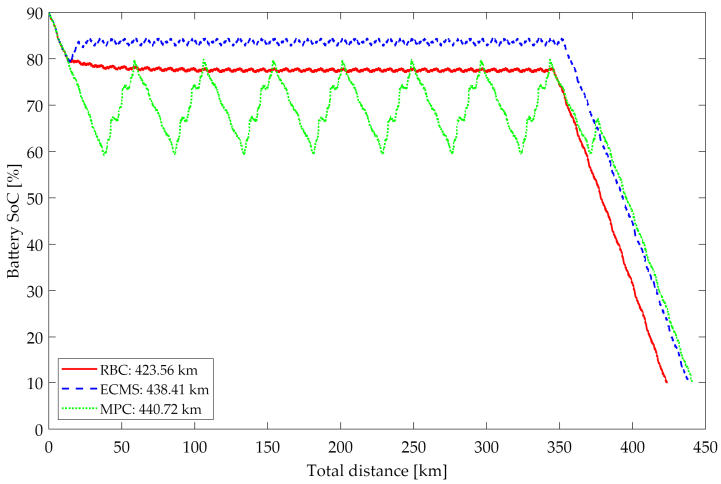

Figure 6. The battery SoC vs. total distance for the three control strategies.

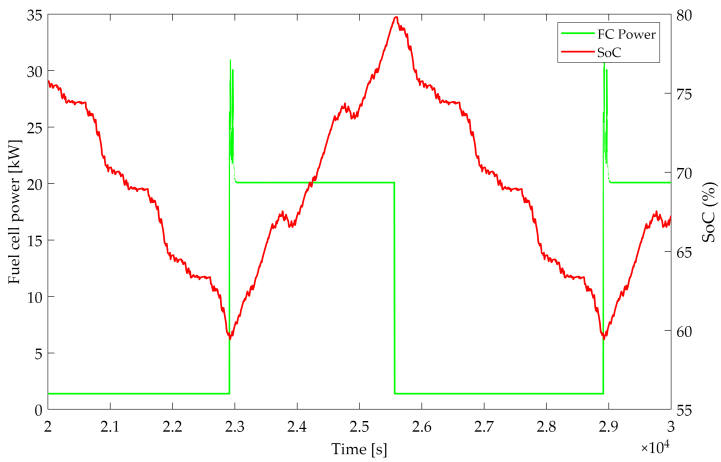

Figure 7. FC power and SoC variation under MPC presented via zoomed-in view.

To prevent unnecessary fuel consumption and battery overcharging when the SoC is sufficient, the FC is commanded to an idle state. Due to the inherent non-continuous operating range of the fuel cell (where stable operation is only guaranteed between 20 and 70 kW), a safety check block in the VCU overrides the MPC signal when the demand falls below the 20 kW threshold, forcing the FC into a 1.5 kW idle mode. It is observed that the FC remains in idle as the SoC decreases from 80% to 60%, because MPC's cost function penalizes the significant power jump from 1.5 kW to 20 kW. To avoid frequent mode switching and its associated high costs, the controller delays reactivation until it is strictly necessary. Once the SoC drops to the 60% lower bound, MPC increases the power command to prevent a violation of the state constraints. This causes the control signal to cross the 20 kW threshold, triggering a transition from idle to the active high-efficiency zone.

The transient spikes in Figure 7 during these transitions stem from a momentary mismatch between MPC's internal state and the VCU's safety override conditions. During the idle phase, the discrepancy between MPC's theoretical output and the FC's actual idle power can lead to minor cumulative errors in the controller's internal logic. Upon reactivation, these errors manifest as brief oscillations. These spikes persist for only approximately 80 s and can be further mitigated by power electronics or software filters in practical applications, making them acceptable for the preliminary research stage.

This periodic switch between active and idle states allows for a comprehensive evaluation of the system dynamics across both steady-state power generation and non-generating phases.

Figure 8 shows the FC power fluctuations both with RBC and the ECMS, with the FC frequently switching between idle and active states. Although FC degradation is not explicitly modeled, such controls are harmful to the FC lifespan [63,64]. In contrast, when governed by the MPC strategy, the FC operates in a quasi-steady manner, with the output power maintained at approximately 20 kW.

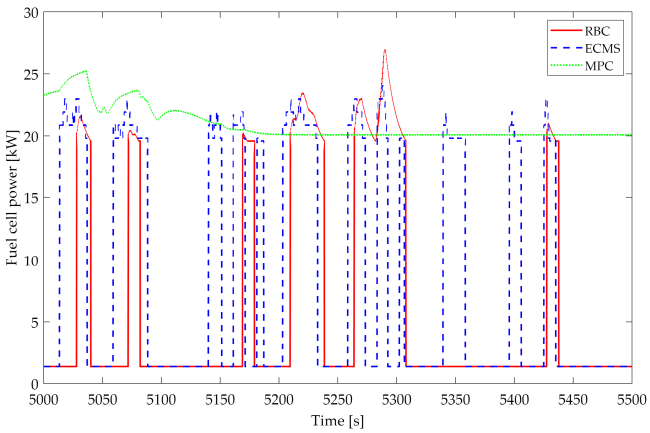

Figure 8. FC power for the three control strategies presented via a zoomed-in view.

This rapid switch arises from two main factors. First, neither RBC nor the ECMS explicitly constrains the upper SoC limit, which may result in sustained FC charging and subsequent VCU intervention when overcharge conditions are approached. Second, to maximize driving range and overall energy efficiency, a relatively high SoC reference is adopted, further increasing the likelihood of VCU intervention under RBC and the ECMS. In contrast, MPC exploits its predictive structure to regulate charging behavior proactively, avoiding VCU intervention even at high SoC levels. Additionally, MPC operates over a wider effective SoC range, allowing the FC to deliver near-constant power for extended periods, thereby improving efficiency and reducing component degradation.

The characteristics of the battery, including its high-rate capability, position it as a more effective solution than the FC for handling rapid power transients. Given that the current study focuses only on power management and does not incorporate battery degradation or life cycle analysis, the results consistently show the battery acting as a power buffer across all three implemented control strategies. A key distinction observed in Figure 9 is that when the FC is active, MPC maintains a more continuous charging profile for the battery. Importantly, none of the three control methods exceed the battery's rated operational limits.

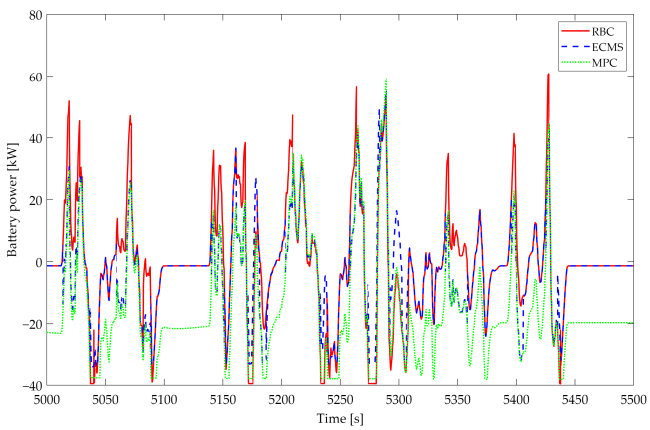

Figure 9. Battery power with FC in active state for three control strategies.

Owing to its superior high-rate capability, the battery is more suitable than the FC for handling rapid power transients. Since this study addresses only the control strategies that regulate FC power only, the battery operates as a power buffer across all three strategies. In Figure 9, MPC does not impose a higher transition load on the battery compared with RBC and the ECMS. Instead, by exploiting its predictive formulation, MPC enables FC charging during low-demand periods, a behavior rarely observed under the other two strategies. This indicates that MPC improves energy availability without increasing battery stress while maintaining operation within rated limits.

Figure 10 illustrates that the battery power output under MPC is higher than that of the other two algorithms while the fuel cell remains idle. These results confirm that the battery consistently operates within its rated limits, ensuring that the MPC strategy maintains vehicle performance. The battery load remains manageable compared to RBC and the ECMS, validating that MPC ensures system reliability without imposing a disproportionate burden on the ESS.

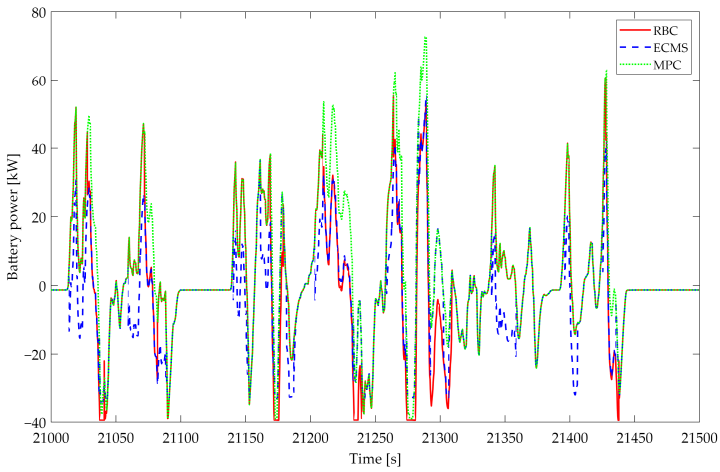

Figure 10. Battery power with FC in idle state for three control strategies.

The efficiency distributions in Figure 11 highlight fundamental differences in the operating philosophies of the three control strategies. RBC exhibits the widest FC power span, extending up to 34 kW, as FC output is directly dictated by the instantaneous ESS power demand. As a result, RBC frequently operates in higher-power regions where FC efficiency deteriorates, particularly above 28 kW. This behavior explains its lower average efficiency and underscores the limitations of rule-based approaches in decoupling FC operation from load fluctuations.

The ECMS demonstrates a more concentrated operating pattern, with most operating points clustered in the 20–24 kW range where FC efficiency is maximized. This reflects the local optimization nature of the ECMS, which favors instantaneous efficiency gains through the equivalence factor formulation. However, the residual spread in operating points indicates that the ECMS remains sensitive to instantaneous demand variations and discretization effects.

MPC achieves the most compact and efficient operating distribution, primarily confined to the high-efficiency region between 20 and 26 kW. The close alignment of its mean operating points with the optimal efficiency curve indicates that predictive optimization effectively anticipates future power demands and exploits the battery as a buffering element. This enables MPC to maintain FC operation near its optimal trajectory while minimizing efficiency degradation, highlighting its superior capability for coordinated energy management in hybrid FC systems.

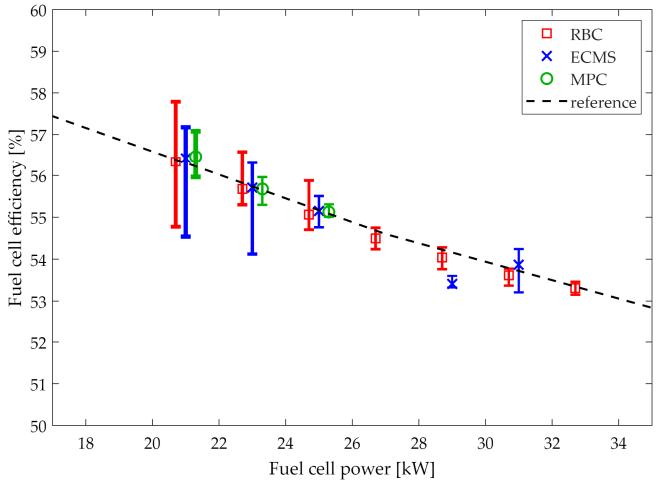

Figure 11. FC efficiency vs. FC power for three control strategies with reference curve.

The operating points located above or below the reference value are mainly caused by transient behavior of the FC. Since its voltage cannot change instantaneously, efficiency decreases during transitions from high to low power, while sudden startups cause the calculated efficiency to increase. Both RBC and the ECMS show a significant number of such transient conditions, which are harmful to the FC's lifetime. Moreover, the model assumes stoichiometric conditions, where $\lambda = 1$ is required to obtain these values. In practical operation, the FC has its own hydrogen flow control during power transients, and the real efficiency is lower than the calculated one.

MPC exhibits the smallest operating range and maintains a relatively smooth power profile, with fewer rapid transitions that could negatively affect component durability.

5. Adaptivity and Robustness

Although Section 3 demonstrated the optimal performance of the three algorithms under the WLTC City cycle, this success should be considered in light of the fact that optimizing for a single condition is often insufficient [65]. This single-cycle optimization approach shows a key limitation: when the vehicle operates under off-design conditions that deviate from the prescribed cycle, its energy efficiency and performance can decline markedly, leading to a noticeable gap relative to real-world user experience [66]. Inspired by this challenge, the present study aims to systematically evaluate the robustness of different EMS algorithms and their performance under off-design conditions by simulating a diverse set of driving scenarios that more closely resemble real-world usage. While the real-world driving scenario generation [28] is complex and time-consuming, a comparative testing approach was adopted to efficiently verify the controller's robustness and generalization capability. Specifically, the Drive Cycle Source block within the Simulink environment was utilized to create a test set comprising 50 representative, non-modal speed profiles.

To characterize the diversity of the off-design driving conditions, the main statistical ranges of the selected 50 driving cycles are summarized here. The average vehicle speed spans from 16.8 km/h to 82.7 km/h, while the maximum speed ranges from 40.9 km/h to 131.3 km/h. The proportion of idle operation (vehicle speed equal to zero) varies significantly, from 0% to 65.35%, reflecting different stop-and-go intensities. The individual cycle lengths range from 1.01 km to 37.14 km. It should be noted that, in the robustness analysis, each driving cycle is repeatedly executed until the available onboard energy is fully depleted; therefore, the final performance comparison is based on the total achievable driving distance rather than the length of a single driving cycle.

All three EMS algorithms were simulated and compared under identical vehicle models, constraints, and test conditions, with the goal of reflecting their true performance differences when facing diverse and challenging driving conditions.

Figure 12 illustrates the performance of the three control algorithms across 50 driving cycles. For the same total available energy, the achievable driving distance varies substantially, from approximately 100 km to 700 km. By recording the remaining hydrogen and battery SoC at the end of each cycle, it is possible to verify whether the EMS operated effectively throughout the test.

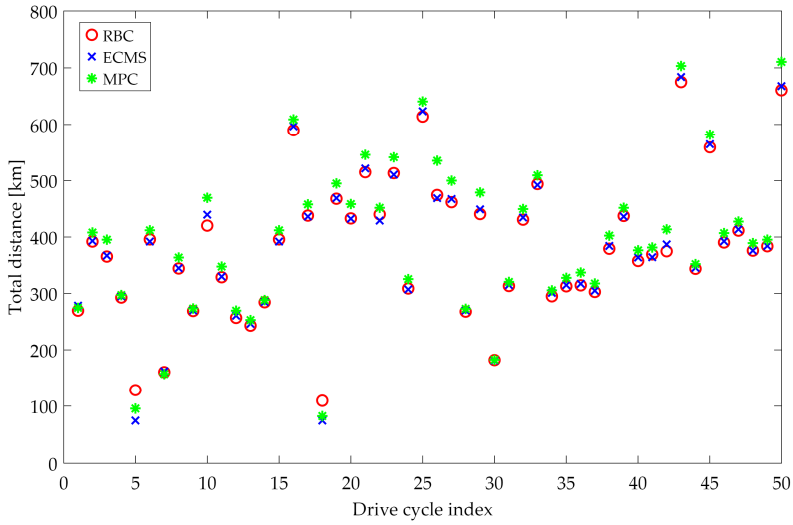

Figure 12. Total driving distance across 50 cycles for the three control strategies.

Due to ESS design constraints and LCV classification, high-speed and motorway drive cycles impose power demands exceeding the FC capability to recharge the battery quickly. This causes the battery to reach its lower operational limit (10% SoC) and terminate the simulation in drive cycles covering less than 200 km. As these cycles exceed the designed capabilities of LCVs, they were excluded from the analysis. The discussion thus focuses exclusively on cycles exceeding 200 km, as these fully deplete the ESS and provide a representative evaluation of the EMS behavior.

The improvement achieved by the MPC strategy is quantified by dividing the additional distance traveled, relative to either RBC or the ECMS, by the corresponding total distance of RBC or the ECMS. A value of 0% therefore represents the MPC performance relative to its own reference. Figure 13 shows that among all evaluated cycles, only one exhibits slightly lower performance for MPC compared with the ECMS. On average, MPC achieves an improvement of approximately 5%, indicating strong robustness and the ability to maintain high energy efficiency even under different driving cycles.

In the region between 400 km and 500 km, a noticeable performance advantage is observed. These cycles can be considered similar to the target WLTC City speed profile.

The frequency distribution presented in Figure 14 illustrates the range of benefits offered by MPC and reveals critical characteristics regarding the shape of its performance distribution. The MPC vs. RBC performance distribution exhibits a relatively wide, right-skewed characteristic, with the primary concentration falling within the 4% to 6% improvement bracket yet featuring a wide spread extending to 8% to 10% and even higher improvement margins (up to approximately 13% to 14%).

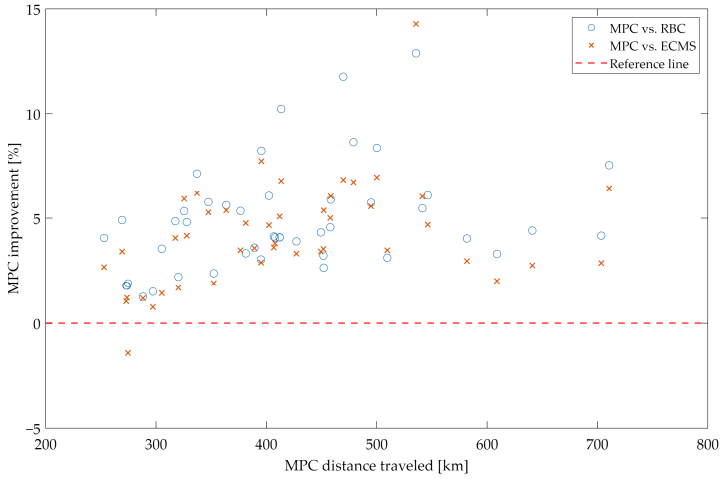

Figure 13. MPC improvement vs. MPC distance of RBC and ECMS.

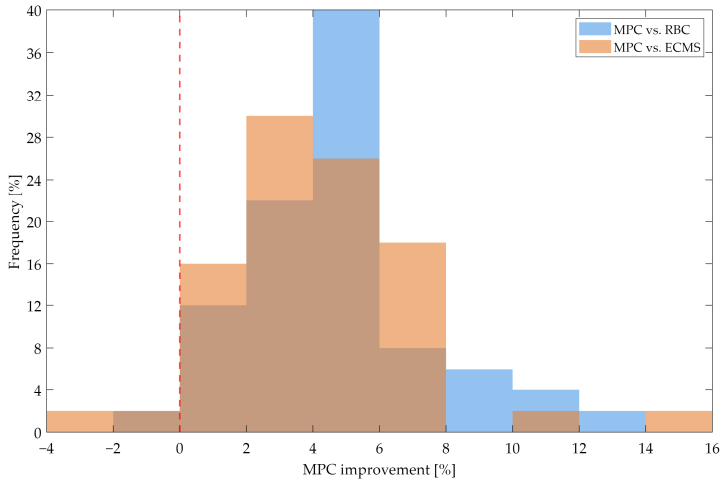

Figure 14. Frequency distribution of relative improvement in performance achieved by MPC compared to RBC and ECMS.

This relatively wide distribution shape suggests a degree of variability in the extent to which MPC outperforms RBC across different speed profiles, though most cases achieve positive gains with extremely rare negative outcomes, demonstrating its universal effectiveness and significant energy-saving potential across various driving cycles. In contrast, the MPC vs. ECMS performance distribution appears more centralized and displays a distinct right-skewed characteristic, with its primary mode located in the 2% to 4% bracket and a secondary mode in the 4% to 6% bracket, resulting in an overall tighter distribution. This centralized distribution shape indicates that because the ECMS is inherently an optimization-based strategy, the marginal benefit derived from MPC is relatively stable and moderate, exhibiting lower volatility.

Figure 15 illustrates the distribution of all possible ranking outcomes across the fifty off-design driving cycles, in terms of total driving distance. The most frequent performance ranking observed is MPC > ECMS > RBC, indicating that the total distance achieved by MPC exceeds that of the ECMS, which in turn overtakes that of RBC. This trend also reflects the relative robustness of the three algorithms: RBC relies on heuristic rules that are not tailored to a specific driving cycle, while the ECMS and MPC incorporate adaptive elements.

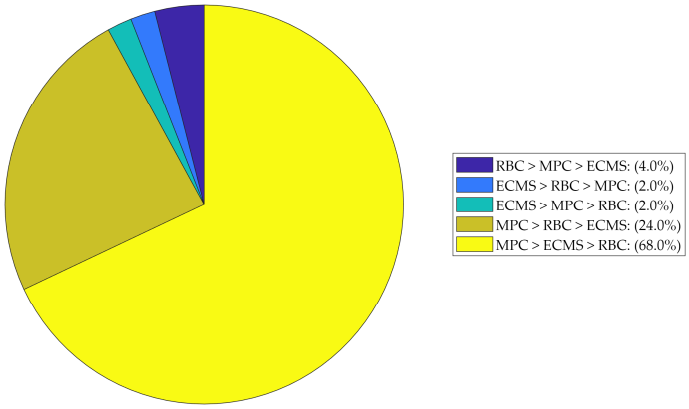

Figure 15. The performance ranking distribution of the three control strategies.

Although the ECMS is typically characterized by limited robustness, the adaptive ECMS designed in this study demonstrates substantially improved performance across diverse cycles. MPC achieves the best overall results, primarily due to its predictive model structure. In addition, the prediction matrices are continuously updated using information from the vehicle CAN bus, which enhances model reliability and enables the controller to maintain superior performance under varying off-design conditions.

6. Conclusions

This study presented a hardware-constrained, physics-consistent evaluation benchmark for FCEV energy management, comparing three strategies, RBC, an adaptive ECMS, and MPC, on an industrial light commercial vehicle prototype. Rather than proposing a new algorithm, the contribution lies in establishing a rigorous and replicable assessment framework that explicitly enforces two VCU-level hardware constraints absent from most existing comparisons: a discontinuous FC operating domain and a mandatory 10 s minimum dwell-time. These constraints fundamentally shape controller behavior and make direct benchmarking against prior published results inapplicable without a dedicated evaluation platform.

Under identical initial energy conditions and across both the target WLTC City cycle and 50 off-design driving scenarios, MPC consistently achieved the longest total driving distance, with an average improvement of approximately 5% over RBC. Its predictive structure enabled the proactive management of FC mode transitions, reducing power fluctuations and improving ESS utilization. The adaptive ECMS also demonstrated strong robustness beyond its calibration cycle, significantly outperforming conventional ECMS implementations. RBC, while serving as a practical industrial baseline, showed limited adaptability under off-design conditions.

The robustness evaluation methodology, unified energy constraints, total driving distance as an unbiased metric, and systematic testing across diverse speed profiles constitute a generalizable validation protocol applicable to future EMS comparisons beyond the specific platform studied here.

To further enhance the proposed strategies, it is recognized that fuel cell lifespan is significantly affected by temperature sensitivity and dynamic operating conditions. By integrating an adaptive temperature compensation strategy based on the SoH [48], the degradation caused by power fluctuations can be further reduced, improving the long-term robustness of MPC.

Future work may integrate battery and FC degradation models and extend the control framework toward HIL testing and VCU integration, supporting the transition from simulation toward operational validation.

Author Contributions: Conceptualization, Z.G., E.G., H.d.C.P., M.C.; methodology, Z.G., E.G., H.d.C.P.; software, Z.G., E.G.; validation, Z.G., E.G.; formal analysis, Z.G., E.G.; investigation, Z.G., E.G.; resources, H.d.C.P., M.C.; data curation, Z.G., E.G.; writing—original draft preparation, Z.G.; writing—review and editing, E.G., H.d.C.P., M.C.; visualization, Z.G., E.G.; supervision, H.d.C.P., M.C.; project administration, M.C.; funding acquisition, M.C. All authors have read and agreed to the published version of the manuscript.

Funding: This research was funded by the European Union—Next Generation EU—PNRR M4C2, Investimento 1.4—Avviso n. 3138 del 16/12/2021—CN00000023 Sustainable Mobility Center (Centro Nazionale per la Mobilità Sostenibile)—CNMS—CUP E13C22000980001.

Data Availability Statement: The original contributions presented in this study are included in the article. Further inquiries can be directed to the corresponding author.

Acknowledgments: During the preparation of this study, the authors used Gemini Deep Research 3.0 for literature review and Claude 4.0 for coding assistance. The authors reviewed and edited all outputs and take full responsibility for the content of this publication.

Conflicts of Interest: The authors declare no conflicts of interest.

Abbreviations and Nomenclature List

The following abbreviations are used in this manuscript:

AI	Artificial Intelligence
DP	Dynamic Programming
ECMS	Equivalent Consumption Minimization Strategy
EMS	Energy Management Strategy
ESS	Energy Source System
FC	Fuel Cell
FCEV	Fuel Cell Electric Vehicle
HIL	Hardware in Loop
LCV	Light Commercial Vehicle
MPC	Model Predictive Control
PCU	Power Control Unit
PMP	Pontryagin's Minimal Principle
RBC	Rule-Based Control
RL	Reinforcement Learning
RSM	Response Surface Methodology
SoC	State of Charge
SoH	State of Health
SoH_2	State of Hydrogen
VCU	Vehicle Control Unit
VDS	Vehicle Dynamic System
WLTC	Worldwide Harmonized Light-Duty Test Cycle
ZOH	Zero-Order Hold

The following variables are used in this manuscript:

Symbol	Meaning	Unit
A	Longitudinal resistive force coefficient	N
B	Longitudinal resistive force coefficient	N/(km/h)
C	Longitudinal resistive force coefficient	$N/(km/h)^2$
C_{bat}	Battery capacity	Ah
F	Faraday number	C/mol
F_{xr}	Longitudinal resistive force	N
M	Vehicle mass	ton
M_{H_2}	Molecular mass of hydrogen	g/mol
N_p	Prediction horizon for MPC	steps

P_{bat}	Battery power	W
P_{elec}	Electric motor power	W
P_{FC}	Fuel cell stack power	W
P_{mech}	Mechanical power	W
P_{req}	DC source required power	W
Q_L	Lower heating value of hydrogen	MJ/kg
R_{int}	Battery internal resistance	mΩ
T_{em}	E-drive output torque	N·m
T_{lim}	Maximum tractive torque	N·m
V_{ref}	Reference vehicle speed	m/s
a_v	Longitudinal acceleration	m/s^2
cmd	Longitudinal controller command	-
h_{CG}	Height of the center of gravity	M
i_{bat}	Battery current	A
i_{FC}	Fuel cell current	A
l	Wheelbase	mm
$\dot{m}_{H_2}$	Hydrogen mass flow rate	g/s
n	Number of fuel cells	-
p	Penalty factor for ECMS	-
r_w	Wheel radius	M
s	Equivalence factor for ECMS	-
v_{bat}	Battery terminal voltage	V
v_{FC}	Fuel cell voltage	V
v_{nom}	Battery open circuit (nominal) voltage	V
α	Road slope angle	rad
λ	Stoichiometric ratio for FC operation	-
η_{DC-DC}	DC-DC converter efficiency	%
η_{em}	E-drive efficiency	%
η_{FC}	Fuel cell system total efficiency	%
μ_x	Road–tire friction coefficient	-
ω_{em}	E-drive rotational speed	rpm

References

1. Mench, M.M. *Fuel Cell Engines*; Wiley: Chichester, UK, 2008.
2. Meng, X.; Liu, M.; Mei, J.; Li, X.; Grigoriev, S.; Hasanien, H.M.; Tang, X.; Li, R.; Sun, C. Polarization loss decomposition-based online health state estimation for proton exchange membrane fuel cells. *Int. J. Hydrogen Energy* **2025**, *157*, 150162. [CrossRef]
3. Meng, X.; Sun, C.; Mei, J.; Tang, X.; Hasanien, H.M.; Jiang, J.; Fan, F.; Song, K. Fuel cell life prediction considering the recovery phenomenon of reversible voltage loss. *J. Power Sources* **2025**, *625*, 235634. [CrossRef]
4. Larminie, J.; Dicks, A.; McDonald, M.S. *Fuel Cell Systems Explained*, 2nd ed.; John Wiley & Sons Ltd.: Hoboken, NJ, USA, 2003.
5. Guzzella, L.; Sciarretta, A. *Vehicle Propulsion Systems: Introduction to Modeling and Optimization*; Springer: Berlin/Heidelberg, Germany, 2013; pp. 1–409. [CrossRef]
6. Carello, M.; Pinheiro, H.D.C.; Longega, L.; Di Napoli, L. Design and Modelling of the Powertrain of a Hybrid Fuel Cell Electric Vehicle. *SAE Tech. Pap. Ser.* **2021**, *3*, 2878–2892. [CrossRef]
7. Han, S.; Zhang, F.; Xi, J. A Real-Time Energy Management Strategy Based on Energy Prediction for Parallel Hybrid Electric Vehicles. *IEEE Access* **2018**, *6*, 70313–70323. [CrossRef]
8. Huang, B.; Yu, W.; Ma, M.; Wei, X.; Wang, G. Artificial-Intelligence-Based Energy Management Strategies for Hybrid Electric Vehicles: A Comprehensive Review. *Energies* **2025**, *18*, 3600. [CrossRef]
9. Wang, D.; Zheng, W.; Wang, Z.; Wang, Y.; Pang, X.; Wang, W. Comparison of reinforcement learning and model predictive control for building energy system optimization. *Appl. Therm. Eng.* **2023**, *228*, 120430. [CrossRef]
10. Guo, Z.; Grano, E.; Mazzeo, F.; Pinheiro, H.d.C.; Carello, M. Calibration and Validation of a PEM Fuel Cell Hybrid Powertrain Model for Energy Management System Design. *Designs* **2025**, *9*, 94. [CrossRef]
11. Behzadi, A.; Alirahmi, S.M.; Yu, H.; Sadrizadeh, S. An efficient renewable hybridization based on hydrogen storage for peak demand reduction: A rule-based energy control and optimization using machine learning techniques. *J. Energy Storage* **2023**, *57*, 106168. [CrossRef]

12. Mohammed, A.S.; Atnaw, S.M.; Salau, A.O.; Eneh, J.N. Review of optimal sizing and power management strategies for fuel cell/battery/super capacitor hybrid electric vehicles. *Energy Rep.* **2023**, *9*, 2213–2228. [CrossRef]
13. Peng, H.; Li, J.; Thul, A.; Deng, K.; Ünlübayir, C.; Löwenstein, L.; Hameyer, K. A scalable, causal, adaptive rule-based energy management for fuel cell hybrid railway vehicles learned from results of dynamic programming. *eTransportation* **2020**, *4*, 100057. [CrossRef]
14. Yuan, H.-B.; Zou, W.-J.; Jung, S.; Kim, Y.-B. Optimized rule-based energy management for a polymer electrolyte membrane fuel cell/battery hybrid power system using a genetic algorithm. *Int. J. Hydrogen Energy* **2022**, *47*, 7932–7948. [CrossRef]
15. Shi, J.; Xu, B.; Zhou, X.; Hou, J. A cloud-based energy management strategy for hybrid electric city bus considering real-time passenger load prediction. *J. Energy Storage* **2022**, *45*, 103749. [CrossRef]
16. Ettihir, K.; Boulon, L.; Agbossou, K. Optimization-based energy management strategy for a fuel cell/battery hybrid power system. *Appl. Energy* **2016**, *163*, 142–153. [CrossRef]
17. Zhang, L.; Liao, R.; Wei, X.; Huang, W. PMP method with a cooperative optimization algorithm considering speed planning and energy management for fuel cell vehicles. *Int. J. Hydrogen Energy* **2024**, *79*, 434–447. [CrossRef]
18. Wang, Y.; Moura, S.J.; Advani, S.G.; Prasad, A.K. Power management system for a fuel cell/battery hybrid vehicle incorporating fuel cell and battery degradation. *Int. J. Hydrogen Energy* **2019**, *44*, 8479–8492. [CrossRef]
19. Zhao, K.; He, K.; Liang, Z.; Mai, M. Global Optimization-Based Energy Management Strategy for Series–Parallel Hybrid Electric Vehicles Using Multi-objective Optimization Algorithm. *Automot. Innov.* **2023**, *6*, 492–507. [CrossRef]
20. Choi, K.; Byun, J.; Lee, S.; Jang, I.G. Adaptive Equivalent Consumption Minimization Strategy (A-ECMS) for the HEVs with a Near-Optimal Equivalent Factor Considering Driving Conditions. *IEEE Trans. Veh. Technol.* **2022**, *71*, 2538–2549. [CrossRef]
21. Tarhini, F.; Talj, R.; Doumiati, M. Holistic adaptive energy-efficient MPC architecture for multi-objective control in over-actuated autonomous vehicles. *Control Eng. Pract.* **2025**, *164*, 106464. [CrossRef]
22. Iqbal, M.; Benmouna, A.; Becherif, M. Data-Driven Modelling and Simulation of Fuel Cell Hybrid Electric Powertrain. *Hydrogen* **2025**, *6*, 53. [CrossRef]
23. Xiao, X.; Shu, C.; Dong, H.; Tang, Y.; Feng, J.; Yuan, H.; Bai, S.; Zhu, S.; Li, G. Weighting Optimization for Fuel Cell Hybrid Vehicles: Lifetime-Conscious Component Sizing and Energy Management. *Appl. Sci.* **2025**, *15*, 3586. [CrossRef]
24. He, P.; Zhang, Q.; Mu, Y.; Qu, Z.; Yin, J.; Li, Z.; Chen, J.; Tao, W.-Q. Temperature-dependent cathode starvation effects on cold start behavior of PEMFC stacks: An experimental investigation. *Appl. Energy* **2026**, *406*, 127299. [CrossRef]
25. Chavan, S.L. Response Surface Methodology Approach for Modeling and Performance Optimization of a PEM Fuel Cell. *Int. J. Autom. Smart Technol.* **2024**, *14*, 45–54. [CrossRef]
26. Kahveci, E.E.; Taymaz, I. Hydrogen PEMFC stack performance analysis through experimental study of operating parameters by using response surface methodology (RSM). *Int. J. Hydrogen Energy* **2022**, *47*, 12293–12303. [CrossRef]
27. Pereira, D.F.; Lopes, F.D.C.; Watanabe, E.H. Nonlinear Model Predictive Control for the Energy Management of Fuel Cell Hybrid Electric Vehicles in Real Time. *IEEE Trans. Ind. Electron.* **2021**, *68*, 3213–3223. [CrossRef]
28. Grano, E.; Villani, M.; Pinheiro, H.d.C.; Carello, M. Are We Testing Vehicles the Right Way? Challenges of Electrified and Connected Vehicles for Standard Drive Cycles and On-Road Testing. *World Electr. Veh. J.* **2025**, *16*, 94. [CrossRef]
29. Zhang, F.; Hua, M.; Zhou, Q.; Wang, S.; Zhang, C.; Du, S.; Duan, Y.; Williams, H.; Xu, H. Robustness Optimization of the Energy Management Strategy for a Fuel Cell Vehicle Using Adversary Evolutionary Learning. *IEEE Trans. Transp. Electrif.* **2025**, *11*, 8729–8741. [CrossRef]
30. Shi, J.; Aarsnes, U.J.F.; Tao, S.; Wang, R.; Nærheim, D.; Moura, S. Health-aware energy management for multiple stack hydrogen fuel cell and battery hybrid systems. *Appl. Energy* **2025**, *397*, 126257. [CrossRef]
31. You, Y.; Yang, Z.; Zhuo, H.-Z.; Xu, N.; Liao, L.; Jiang, W. Design of an adaptive MPC control system for unmanned ground vehicle based on FP-ADMM and RBFNN. *Control Eng. Pract.* **2025**, *164*, 106399. [CrossRef]
32. Emission Test Cycles: WLTC. Available online: https://dieselnet.com/standards/cycles/wltp.php (accessed on 26 November 2025).
33. Della Ragione, L.; Meccariello, G. Statistical approach to identify Naples city's real driving cycle referring to the Worldwide harmonized Light duty Test Cycle (WLTC) framework. In *Sustainable Development and Planning VIII*; WIT Press: Southampton, UK, 2016; Volume 1, pp. 555–566. [CrossRef]
34. Lasocki, J. The WLTC vs NEDC: A Case Study on the Impacts of Driving Cycle on Engine Performance and Fuel Consumption. *Int. J. Automot. Mech. Eng.* **2021**, *18*, 9071–9081. [CrossRef]
35. Drive Cycle Source—Standard or Specified Longitudinal Drive Cycle—Simulink. Available online: https://uk.mathworks.com/help/autoblks/ref/drivecyclesource.html (accessed on 9 December 2025).
36. Wang, T.; Cassandras, C.G.; Pourazarm, S. Optimal motion control for energy-aware electric vehicles. *Control Eng. Pract.* **2015**, *38*, 37–45. [CrossRef]
37. Quan, R.; Guo, H.; Li, X.; Zhang, J.; Chang, Y. A real-time energy management strategy for fuel cell vehicle based on Pontryagin's minimum principle. *iScience* **2024**, *27*, 109473. [CrossRef] [PubMed]

38. Islam, A.; Jahan, I.; Farrok, O. Fuel cell hybrid electric vehicle with real-world driving cycle: Six-step control strategy for dynamic energy management and fuel optimization. *Energy Convers. Manag. X* **2026**, *29*, 101435. [CrossRef]
39. Almousa, M.T.; Rezk, H.; Alahmer, A. Optimized equivalent consumption minimization strategy-based artificial Hummingbird Algorithm for electric vehicles. *Front. Energy Res.* **2024**, *12*, 1344341. [CrossRef]
40. Morsi, Y.A.; Hasaneen, K.M.; Abdel-Rahim, N.; Abdelqawee, I.M. A robust energy management strategy for fuel cell and ultracapacitor hybrid electric vehicles under uncertainty via a jellyfish-search-based approach. *Sci. Rep.* **2025**, *15*, 37361. [CrossRef] [PubMed]
41. Wu, Y.; Zheng, W.; Qin, J. Modified P-ECMS for Fuel Cell Commercial Vehicles Based on SSA-LSTM Vehicle Speed Prediction and Integration of Future Speed Trends into Dynamic Equivalent Factor Regulation. *Sustainability* **2025**, *18*, 306. [CrossRef]
42. Grano, E.; Villani, M.; Ahmed, Q.; Carello, M. Leveraging Traffic-in-the-Loop Simulations to Assess the Impact of Traffic on Vehicle Energy Consumption. In *WCX SAE World Congress Experience, Detroit, MI, USA, 8–10 April 2025*; SAE Technical Papers; Society of Automotive Engineers (SAE): North Melbourne, VIC, Australia, 2025. [CrossRef]
43. Wang, C.; Nehrir, M.; Shaw, S. Dynamic Models and Model Validation for PEM Fuel Cells Using Electrical Circuits. *IEEE Trans. Energy Convers.* **2005**, *20*, 442–451. [CrossRef]
44. Adzakpa, K.P.; Agbossou, K.; Dube, Y.; Dostie, M.; Fournier, M.; Poulin, A. PEM Fuel Cells Modeling and Analysis Through Current and Voltage Transient Behaviors. *IEEE Trans. Energy Convers.* **2008**, *23*, 581–591. [CrossRef]
45. Darvishi, Y.; Hassan-Beygi, S.R.; Zarafshan, P.; Hooshyari, K.; Malaga-Toboła, U.; Gancarz, M. Numerical Modeling and Evaluation of PEM Used for Fuel Cell Vehicles. *Materials* **2021**, *14*, 7907. [CrossRef]
46. Omran, A.; Lucchesi, A.; Smith, D.; Alaswad, A.; Amiri, A.; Wilberforce, T.; Sodré, J.R.; Olabi, A. Mathematical model of a proton-exchange membrane (PEM) fuel cell. *Int. J. Thermofluids* **2021**, *11*, 100110. [CrossRef]
47. Song, K.; Hou, T.; Jiang, J.; Grigoriev, S.A.; Fan, F.; Qin, J.; Wang, Z.; Sun, C. Thermal management of liquid-cooled proton exchange membrane fuel cell: A review. *J. Power Sources* **2025**, *648*, 237227. [CrossRef]
48. Tang, X.; Yang, M.; Shi, L.; Hou, Z.; Xu, S.; Sun, C. Adaptive state-of-health temperature sensitivity characteristics for durability improvement of PEM fuel cells. *Chem. Eng. J.* **2024**, *491*, 151951. [CrossRef]
49. He, H.; Xiong, R.; Fan, J. Evaluation of Lithium-Ion Battery Equivalent Circuit Models for State of Charge Estimation by an Experimental Approach. *Energies* **2011**, *4*, 582–598. [CrossRef]
50. Grano, E.; Lazek, T.; Carello, M. A numerical Methodology for Induction Motor Control: Lookup Tables Generation and Steady-State Performance Analysis. In *SAE Technical Papers*; SAE International: Warrendale, PA, USA, 2024. [CrossRef]
51. Gu, J.; Ouyang, M.; Li, J. Vehicle Dynamic Simulation for Efficiency Optimization of Four-wheel Independent Driven Electric Vehicle. *World Electr. Veh. J.* **2010**, *4*, 319–324. [CrossRef]
52. Pinheiro, H.d.C. PerfECT Design Tool: Electric Vehicle Modelling and Experimental Validation. *World Electr. Veh. J.* **2023**, *14*, 337. [CrossRef]
53. Olson, B.J.; Shaw, S.W.; Stépán, G. Stability and Bifurcation of Longitudinal Vehicle Braking. *Nonlinear Dyn.* **2005**, *40*, 339–365. [CrossRef]
54. Singh, S. Longitudinal Velocity Control of Autonomous Ground Vehicle using PID and PI Controller. *Int. J. Res. Appl. Sci. Eng. Technol.* **2021**, *9*, 504–510. [CrossRef]
55. Lee, S.; Eom, I.; Lee, B.; Won, J. Driving Characteristics Analysis Method Based on Real-World Driving Data. *Energies* **2024**, *17*, 185. [CrossRef]
56. Cheng, R.; Zhang, W.; Yang, J.; Wang, S.; Li, L. Analysis of the Effects of Different Driving Cycles on the Driving Range and Energy Consumption of BEVs. *World Electr. Veh. J.* **2025**, *16*, 124. [CrossRef]
57. Sun, W.; Liu, H.; Han, M.; Sun, K.; Bai, S.; Li, G. A Novel Method for the Application of the ECMS (Equivalent Consumption Minimization Strategy) to Reduce Hydrogen Consumption in Fuel Cell Hybrid Electric Vehicles. *Fluid Dyn. Mater. Process.* **2022**, *18*, 867–882. [CrossRef]
58. Torreglosa, J.; Jurado, F.; García, P.; Fernández, L. Hybrid fuel cell and battery tramway control based on an equivalent consumption minimization strategy. *Control Eng. Pract.* **2011**, *19*, 1182–1194. [CrossRef]
59. Zhao, X.; Li, J.; Liu, M.; Zhang, J.; Azad, N.L. An Optimal Energy Management Strategy with Time-Varying Equivalent Factor Based on Transformer for Multi-Mode Hybrid Electric Mining Trucks. *IEEE Open J. Veh. Technol.* **2025**, *6*, 1749–1759. [CrossRef]
60. Couch, J.; Fiorentini, L.; Canova, M. An ECMS-Based Approach for the Energy Management of a Vehicle Electrical System. *IFAC Proc. Vol.* **2013**, *46*, 115–120. [CrossRef]
61. Borhan, H.; Vahidi, A.; Phillips, A.M.; Kuang, M.L.; Kolmanovsky, I.V.; Di Cairano, S. MPC-Based Energy Management of a Power-Split Hybrid Electric Vehicle. *IEEE Trans. Control Syst. Technol.* **2011**, *20*, 593–603. [CrossRef]
62. Wang, G.; Huang, F.; Yu, Y.; Wen, S.; Tu, Z. Degradation behavior of a proton exchange membrane fuel cell stack under dynamic cycles between idling and rated condition. *Int. J. Hydrogen Energy* **2018**, *43*, 4471–4481. [CrossRef]

63. Mazzeo, F.; Di Napoli, L.; Carello, M.; Prokop, M.; Paidar, M.; Bouzek, K. Electrochemical signatures in proton exchange membrane fuel cells: A comprehensive study based on distribution of relaxation times. *Int. J. Hydrogen Energy* **2026**, *202*, 152860. [CrossRef]
64. Pan, Y.; Zhong, K.; Xie, Y.; Pan, M.; Guan, W.; Li, L.; Liu, C.; Man, X.; Zhang, Z.; Li, M. A Review of Hybrid Vehicles Classification and Their Energy Management Strategies: An Exploration of the Advantages of Genetic Algorithms. *Algorithms* **2025**, *18*, 354. [CrossRef]
65. Fontaras, G.; Ciuffo, B.; Zacharof, N.; Tsiakmakis, S.; Marotta, A.; Pavlovic, J.; Anagnostopoulos, K. The difference between reported and real-world CO_2 emissions: How much improvement can be expected by WLTP introduction? *Transp. Res. Procedia* **2017**, *25*, 3933–3943. [CrossRef]
66. Lee, H.; Song, C.; Kim, N.; Cha, S.W. Comparative Analysis of Energy Management Strategies for HEV: Dynamic Programming and Reinforcement Learning. *IEEE Access* **2020**, *8*, 67112–67123. [CrossRef]